PAPER • OPEN ACCESS

Progress in design and experimental activities for the development of an advanced breeding blanket

OPEN ACCESS
IOP Publishing | International Atomic Energy Agency
Nuclear Fusion
Nucl. Fusion **64** (2024) 056029 (16pp)
https://doi.org/10.1088/1741-4326/ad37ca

Progress in design and experimental activities for the development of an advanced breeding blanket

I. Fernández-Berceruelo[1,*], I. Palermo[1], F.R. Urgorri[1], D. Rapisarda[1], M. González[1], J. Alguacil[2], J.P. Catalán[2], J.M. García[1], J. Kekrt[3], M. Kordač[3], I. Krastiņš[4], T. Melichar[3], J.Á. Noguerón[1], E. Platacis[4], R. Petráš[3], M. Roldán[1], A. Rueda[5], J. Serna[5], D. Sosa[1] and D. Suàrez[6,7]

[1] National Fusion Laboratory, CIEMAT, Madrid, Spain
[2] Department of Energy Engineering, ETSII UNED, Madrid, Spain
[3] Rez Research Centre (CVR), Rez, Czech Republic
[4] Institute of Physics, University of Latvia, Riga, Latvia
[5] Empresarios Agrupados Internacional, Madrid, Spain
[6] Department of Physics, Technical University of Catalonia, Barcelona, Spain
[7] Oak Ridge National Laboratory, Oak Ridge, TN, United States of America

E-mail: ivan.fernandez@ciemat.es

Received 14 January 2024, revised 7 March 2024
Accepted for publication 26 March 2024
Published 9 April 2024

Abstract

There is no doubt about the interest of achieving as fast as possible the capability to build and operate high performance reactors that finally allow fusion competing in the electricity market. An advanced breeding blanket based on the Dual Coolant Lithium Lead concept with single module segment architecture, designed for the European DEMO, is certainly aligned with such objective. This work describes some recent outcomes of the efforts carried out in the framework of the Prospective R&D Work Package in EUROfusion to develop this line. The evolution of the design has been guided by strategies aimed to achieve an equilibrium between tritium breeding & shielding requirements and mechanical integrity. To enhance the thermodynamic cycle efficiency and reduce the recirculation power by minimizing pressure losses in both the breeding zone and the first wall have been complementary guidelines. Specific models have been created to characterize phenomena like heat transfer and tritium permeation in the breeder channels. The experimental activities, which in general have produced promising results, have consisted in the characterization of different ceramic materials (carbides and oxides) in terms of functional properties at high temperature (as-received and irradiated/implanted samples) and compatibility with PbLi.

Keywords: advanced breeding blanket, PbLi, dual coolant

(Some figures may appear in colour only in the online journal)

* Author to whom any correspondence should be addressed.

1. Introduction

As one of the most critical systems in a fusion reactor, the Breeding Blanket (BB) must fulfill essential functions, among which ensuring tritium self-sufficiency and extracting most of the fusion power stand out. At the same time, it shall observe ambitious requirements in terms of availability and thermodynamic cycle/electric efficiency if fusion intends to succeed as an attractive option in the electricity pool. Such requirements define what we could call an *advanced BB*.

Through a comprehensive analysis of different alternatives in terms of breeder, coolant, functional materials and circuits topology, a novel conceptual design of an advanced BB with Single Module Segment architecture (SMS) for the European DEMO reactor was proposed in [1, 2].

The following sections summarize recent activities devoted to improve the tritium breeding and shielding capability of the BB segments, as well as consolidating the supporting scheme, optimizing the First Wall (FW) cooling system, modeling tritium transport in the breeder channels and modeling magnetohydrodynamics (MHDs) phenomena (heat transfer in magnetoconvective flows and relationship between wall shear stress and corrosion rates). The results of R&D in materials are also reported in this work.

2. Main characteristics

The current design solution employs the eutectic alloy of Pb and Li as breeder, shielding, neutron multiplier and tritium carrier. PbLi is self-cooled by flowing at relatively high velocity (a few cm s^{-1}), which gives rise to the need of electrically insulating the walls of the liquid metal circuit to minimize the pressure drop due to the coupling between the magnetic and velocity fields in such conductive fluid. This is solved by enclosing the PbLi circuit inside a box made of an electrically resistive and chemically compatible ceramic material. This approach also involves the benefit of reducing the electromagnetic loads transmitted to the structure and making tritium permeation towards the exterior of the box almost negligible.

The box is protected and supported by a EUROFER steel case which includes a helium-cooled FW panel, with a layer of tungsten as plasma facing material. Both components are separated by a gap that absorbs the differential expansion of ceramic and steel at the normal operation temperature. The gap, filled with an inert gas, also provides thermal insulation between them to allow reaching high temperatures in the breeding zone while keeping the limit of 550 °C imposed by creep phenomena in EUROFER [3]. Therefore, the design shares some of the fundamental features of the classical Dual Coolant Lithium Lead (DCLL) BB concept [4], although differs in the lack of Flow Channel Inserts (FCI) and the fact that helium is essentially committed to cool the FW and not the internal plates.

2.1. PbLi circuits

Inside the ceramic box, PbLi follows a simple path in poloidal direction (figure 1). The 3D flow features, whose MHD effects

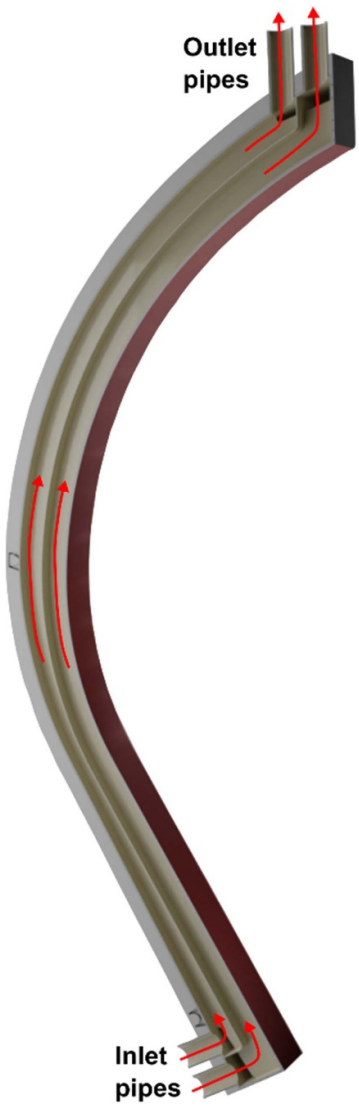

Figure 1. Radial-poloidal section view of the outboard central segment. PbLi paths indicated by red arrows.

cannot be completely mitigated by insulating the surrounding walls, are practically limited to the inlet and outlet regions (flow expansion/contraction and turns around the transitions between the breeding zone and the inlet/outlet pipes). The space is divided into six front and six rear channels with quadrilateral cross-section (figure 2). The rear and front channels are respectively fed by two independent pipes. This way the mass flow rate of both circuits can be adapted to the different nuclear heating values to keep the same outlet temperature.

The inlet pipes are located at the bottom of the segment, so that there is ascending flow in parallel in every channel. This minimizes the risk of reversed flows due to buoyancy forces, since forced flow is buoyancy-assisted, and the problems linked to nucleation and growing of helium bubbles, since these tend to rise [5] and can be transported by advection and extracted by the liquid metal flow. Besides, radial thermal gradients are minimized and displacements are basically produced in poloidal direction. Since the vacuum vessel-BB attachment system can provide higher freedom to expand

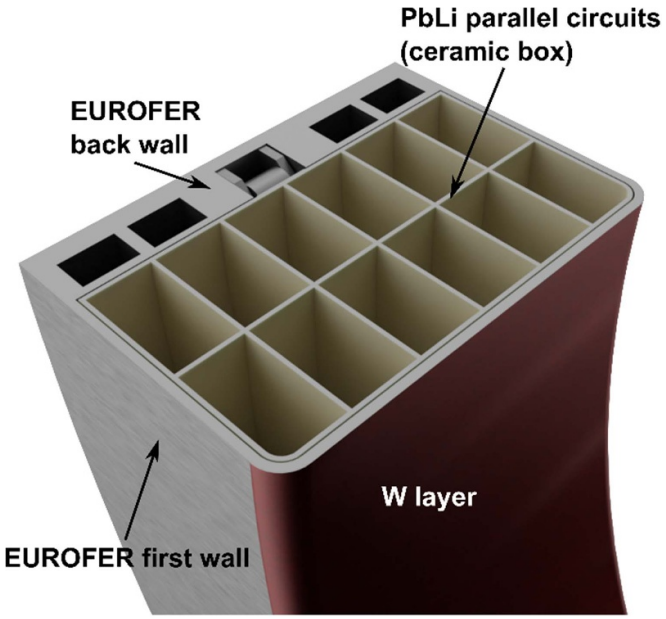

Figure 2. Radial-toroidal section view of the outboard central segment.

Table 1. PbLi average velocity (cm s^{-1}) in the poloidal ducts. OBL stands for outboard lateral segment.

	OBC	OBL	IB
Front channels	4.9	4.7	3.6
Rear channels	1.0	1.0	0.7

in poloidal direction, this arrangement of the PbLi circuits is also favorable to reduce thermal stresses.

Another distinction from other high-temperature DCLL designs is the PbLi inlet temperature, commonly set in the range 350 °C–480 °C [4, 6]. The thermal range selected here (T_{inlet} = 300 °C; T_{outlet} = 700 °C) would allow obtaining a significant value of Carnot's cycle efficiency (60.2%), which is reduced to a still remarkable value of 57.5% when considering the contribution of helium. They have been calculated from the following expression:

$$\eta_C = 1 - \left(\alpha + (1-\alpha)\frac{T_{\text{avg PbLi}}}{T_{\text{avg He}}}\right)\frac{T_{\text{avgsink}}}{T_{\text{avg PbLi}}}$$

where α is the fraction of power extracted by PbLi (0.67) and T_{avg} are the respective average absolute temperatures of PbLi (573–973 K), He (573–682 K) and the sink of the power conversion cycle (298–303 K).

Simultaneously, the large difference between outlet and inlet temperature allows constraining the magnitude of the flow rate (∼1.5 m^3 s^{-1} for the whole reactor). The resulting PbLi average velocities in the poloidal ducts are displayed in table 1. The combination of both circumstances (high outlet temperature and low mass flow rate) is also favorable to improve the recovery of tritium dissolved in the liquid metal, as well as to reduce the corrosion-erosion rate.

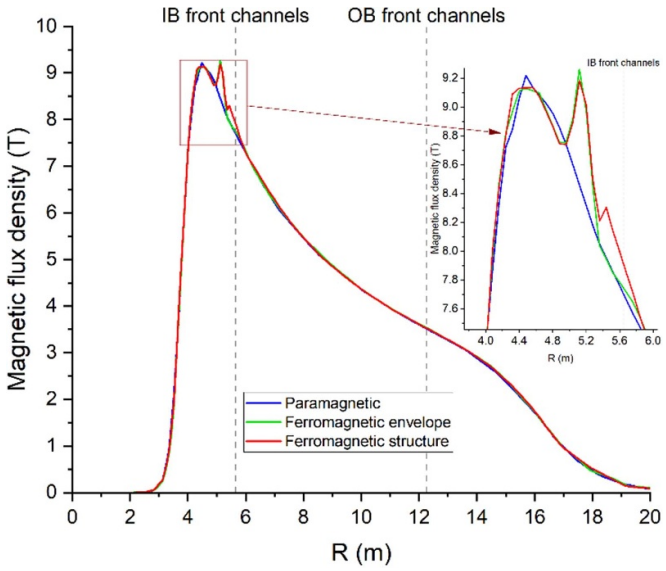

Figure 3. Magnetic flux density at the equatorial level along the radial direction for different configurations of the breeding zone regarding the content of ferromagnetic material in an IB segment. The minor deviations produced in some parts of the profile are caused by small differences in the mesh resolution.

Undoubtedly, the reduced amount of ferromagnetic material, ∼25% smaller than in an analogous design with a coated advanced steel [7], has several advantages from the structural point of view. It implies lower weight and lower steady state magnetic forces due to magnetization. Figure 3 shows the magnetic flux density obtained at the equatorial level along the radial direction for different configurations of the breeding zone regarding the content of ferromagnetic material. It has been obtained from magnetostatic 3D Finite Element (FE) analyses (22.5° sector) carried out in ANSYS APDL, using elements based on the edge-flux formulation. The blue curve represents the magnetic field profile produced by a current density in the Toroidal Field (TF) coils that originates 4.89 T at the major radius (8.938 m) [8] in the absence of ferromagnetic material. The green curve represents the effect of including just one inboard (IB) blanket segment with the EUROFER envelope, whereas the red one corresponds to a hypothetical design variant in which the internal ceramic walls that define the PbLi circuits are substituted by EUROFER. In these cases, non-linear B-H curves have been employed [9]. As can be seen in the detail plot, the magnetization of the surrounding EUROFER plates increases the magnetic field ∼3% in the region of the IB front channels. It is a modest difference that practically has no effect on the MHD phenomena. Apart from that, it has been verified from this model that it would be possible to provide an effective magnetic shielding to the breeder channels by covering them with a material with very high relative magnetic permeability, conveniently separated from PbLi, but such measure is unfeasible from different points of view (e.g. magnetization forces).

It is also worth to mention that this specific configuration, with insulating walls and gap, can help to reduce forces due to eddy currents induced during plasma events, although this

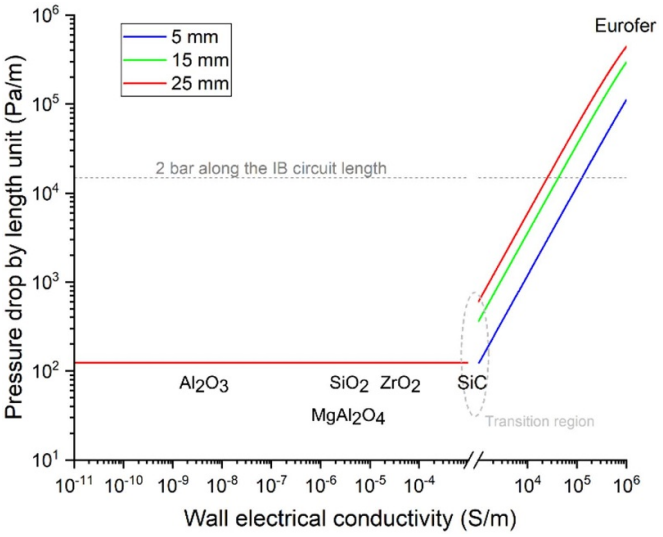

Figure 4. Pressure gradient in the front PbLi channels of the IB segments for a range of wall electrical conductivity (taken at representative T $\sim$ 550 °C–650 °C) and three values of wall thickness.

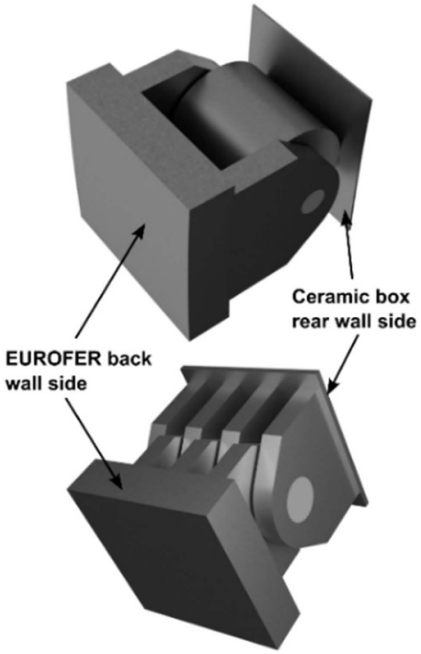

Figure 5. Roller (top) and hinged (bottom) supports.

must be confirmed by specific electromagnetic transient analyses. In any case, the electrical insulation provided by the ceramic box is enough to make pumping in the PbLi loops viable. Figure 4 shows an estimation of the pressure gradient with fully-developed flow in the front PbLi channels of the IB segments, considering a range of wall electrical conductivity and three values of the ceramic wall thickness. The left side of the plot has been obtained using a correlation for perfectly-insulated walls proposed by Shercliff [10]:

$$\partial_z p \left[\frac{Pa}{m}\right] = B_0^2 U_0 \frac{1}{Ha - 0.852\frac{a}{b}\sqrt{Ha} - 1}$$

$$Ha = B_0 a \sqrt{\frac{\sigma}{\eta}}$$

where B_0 is the external magnetic field, U_0 is the PbLi average velocity, σ is the PbLi electrical conductivity, η is the PbLi dynamic viscosity and 2a & 2b are the dimensions of the channel cross-section (a is parallel to the magnetic field). The PbLi properties have been taken from [11].

The right side of the plot has been evaluated through a correlation for non-perfectly conducting walls recommended by Miyazaki *et al* [12]:

$$\partial_z p \left[\frac{Pa}{m}\right] \cong B_0^2 U_0 \sigma \frac{C_w}{1 + \frac{a}{3b} + C_w}$$

$$C_w = \frac{\sigma_w t_w}{\sigma a}$$

where σ_w and t_w are respectively the electrical conductivity and thickness of the walls.

There is a transition region between 10^{-3} and 10^{3} S m^{-1}, approximately, where such correlations are hardly applicable. As can be appreciated, the pressure gradient expected with ceramic walls is low, several orders of magnitude lower than the one calculated with EUROFER and far below the horizontal grey line which indicates the pressure gradient that would lead to a total pressure drop of 2 bar along the IB circuit length (around 13 m). It must be noted here that this is only referred to fully-developed flow along the poloidal channels, and no other contributions to MHD pressure drop (e.g. flow expansions and contractions, turns and fringing magnetic field) have been considered. Nevertheless, 2 bar is quite conservative as pressure drop limit for an IB segment. It must be underlined that even with a total pressure drop of 10 bar in the PbLi loop, the pumping power for the whole reactor would be $<$20 MW.

2.2. *Supporting scheme*

One of the most critical aspects of this design is the mechanical interface between the ceramic box and the steel envelope, since it must provide support for the box, transfer the electromagnetic loads produced inside PbLi by plasma events, and absorb the differential thermal expansion of both components. These functions are accomplished by the combination of a hinged support, located above the inlet pipes, and a roller support, situated at the Center of Gravity (COG) of the segment -approximately at the equatorial level- (figure 5), which create an isostatic supporting condition. The coupled Degrees of Freedom (DOF) between the ceramic box and the EUROFER back wall are depicted in figure 6.

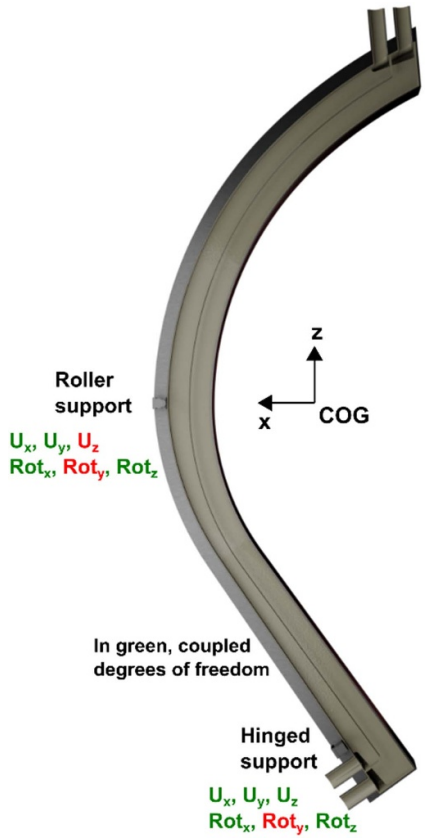

Figure 6. Coupled degrees of freedom between the ceramic box and the EUROFER back wall provided by each support.

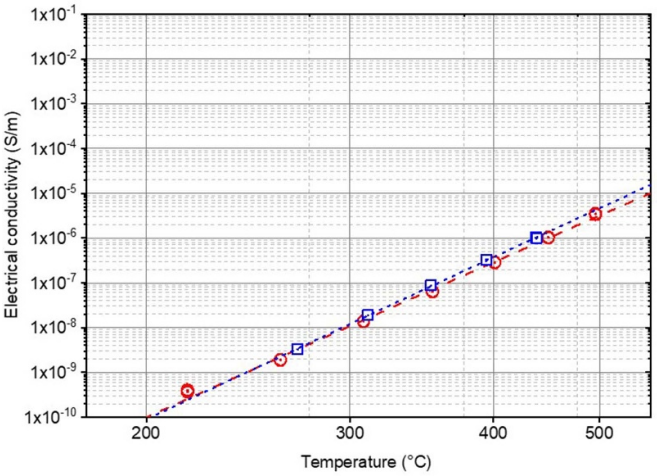

Figure 7. Electrical conductivity of $MgAl_2O_4$ immersed in PbLi as a function of temperature. The red curve has been obtained using a two-electrode arrangement with gold electrodes on both sides of the sample. The blue curve has been obtained using a gold electrode on one side and a PbLi electrode on the other.

3. The ceramic material

The search of candidate ceramic materials with suitable thermophysical, chemical and mechanical properties has been focused on those with neutron activation responses (in particular decay heat, contact dose rate and specific activity) equal or better than EUROFER, for which reason a thorough radiological characterization and classification of 16 compositions was initially made [1, 13]. Among the preliminarily selected, several metal carbides (e.g. TiC), excepting SiC, have been completely discarded after testing due to: (1) the electrical conductivity at relevant temperatures have shown values above 100 S m^{-1}; and (2) their stability has been seriously affected by the dissolution of the solid phases by melted PbLi. However, ceramic oxides have shown optimum microstructure and properties when subjected to radiation and the action of liquid metal.

Thus, most of the R&D activities have been concentrated in silicon carbide and several oxides: alumina (Al_2O_3), zirconia (4–10 mole% Y_2O_3-stabilized ZrO_2), silica (SiO_2) and spinel ($MgAl_2O_4$). They comprise:

(a) Testing of as-received commercial ceramics under representative operating conditions.
(b) Testing of electron-irradiated and ion-implanted commercial ceramics under representative operating conditions.
(c) Development of ceramic-steel connections.

The testing of as-received commercial ceramics has consisted in measuring the electrical conductivity at high temperature, with or without immersion in PbLi, as well as assessing the mechanical behavior inside static PbLi and the chemical compatibility with flowing PbLi under a strong magnetic field. For example, a minor electrical degradation has been observed in Al_2O_3 samples by monitoring their electrical conductivity under polarization (400 V) and thermal cycles between 200 °C and 430 °C [14]. Besides, the surface conductivity values measured at high temperature in $MgAl_2O_4$ (figure 7) and SiO_2 are well below the limit values suggested by figure 4.

It has been found that the surface microstructure of Al_2O_3 is slightly altered after 1000 h inside static PbLi at 550 °C. The grain boundary phase of the first 10–15 μm is partially lost, which provokes the penetration of Li. A degradation rate of 88 μm y^{-1} has been calculated. In the case of ZrO_2, a small surface degradation has been detected, but it is not comparable to Al_2O_3. The spinel samples have been attacked by the liquid metal, provoking a selective removal of Al from the surface and an enrichment in Mg by diffusion from the bulk. It has been estimated a degradation rate of 66 μm y^{-1}.

Additionally, Al_2O_3 and Si-infiltrated SiC samples have been tested after being immersed in flowing PbLi at 550 °C during 500 h, under a transverse magnetic field of 5 T. The results have shown a very good compatibility with PbLi. Only an area enriched in Ni and completely depleted in Si in the Si-SiC composite has been observed [15].

There is also a right preservation of mechanical properties as nanoindentation hardness, Young's modulus or flexural strength at high temperature (e.g. flexural strength of Al_2O_3 samples at 650 °C is ∼10% lower than that of samples at room temperature [16]), with non-pronounced impact of PbLi wetting.

As mentioned, some samples have been subjected to accelerated ion implantation (He+ beam, H+ beam or sequential co-implantation by He+ and H+ beams). It has been observed

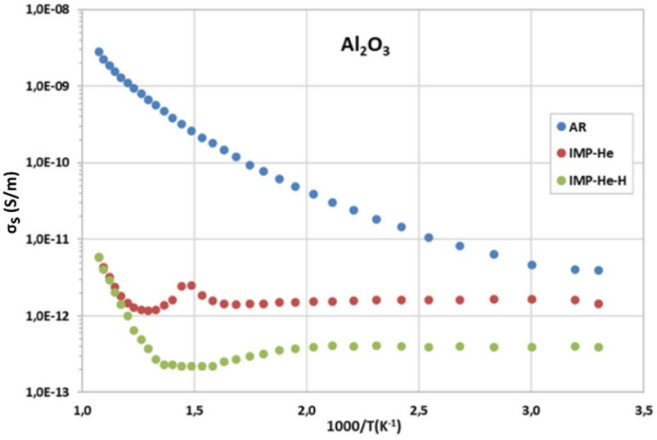

Figure 8. Surface electrical conductivity of Al_2O_3 samples (as-received and implanted) as a function of temperature.

that the volume electrical conductivity of ZrO_2 increases up to a limit of 10^{-4} S m^{-1} when it is irradiated with electron beam up to 4 MGy. Nonetheless, it is worth to underscore the lower increase of the electrical conductivity at high temperature of ion-implanted samples with respect to as-received (figure 8), due to trapping or blocking of charge carriers in the generated gas cavities [17], whereas the studied mechanical properties of such samples remain similar [18]. In Al_2O_3 ion-implanted samples, the formation of $LiAlO_2$ in the layer affected by PbLi has been noticed, with a slight influence of implantation on the attack kinetics [19]. The next campaign will be focused on ZrO_2, SiO_2 and $MgAl_2O_4$. Furthermore, due to the good behavior of ion-implanted samples, an irradiation campaign with heavy and light ions (D and He) has started in order to simulate neutron-like damage and transmutation by-products.

Finally, considering the need of developing ceramic-steel connections, Al_2O_3 tubes have been successfully joined to steel flanges by brazing, using Ag and Cu-based filler metals. They have been subjected to thermal shock and high temperature during several hours. Both the microstructure and hardness values (indentation) have remained stable in the vicinity of the joints.

4. The double-wall challenge

The double wall (ceramic + gap + steel) plays a key role from the points of view of operation and safety (plasma-facing component, containment, electrical insulation, corrosion and permeation barrier). Nevertheless, its whole thickness supposes a challenge to fulfill the required Tritium Breeding Ratio (TBR), currently established in 1.15 within the EUROfusion DEMO Programme [20]. The ceramic box has no structural function, but it must withstand its own weight and electromagnetic and pressure loads, so the balance between tritium production and mechanical strength is delicate. It is necessary a trade-off, which can be attained from the coordination of neutron transport analyses (MCNP5 [21]) and mechanical integrity analyses (ANSYS APDL). Because of dealing with brittle materials, the ceramic box integrity assessment follows an approach based on the Weibull probability distribution, which can be obtained from statistics of fracture mechanics [22]. The probability of failure is given by the following expression:

$$F = 1 - \exp\left(-\frac{1}{V_0}\int\left(\frac{\sigma_e}{\sigma_0}\right)^m \mathrm{d}V\right)$$

where m is the Weibull modulus-depending exclusively on the size frequency density of cracks in a specimen-, σ_0 is the characteristic strength for a reference volume V_0 and σ_e is an equivalent stress calculated according to the Principle of Independent Action (PIA) [22]:

$$\sigma_e = (\sigma_1^m + \sigma_2^m + \sigma_3^m)^{1/m}$$

where σ_1, σ_2 and σ_3 are the principal stresses, if they are positive (otherwise, a null value is adopted).

The 3D FE analyses have been focused on the Outboard Central Segment (OBC). They use multi-layer (ceramic box) and single layer (steel envelope) linear shell elements. The connection between both components is achieved by means of two pairs of duplicated extra nodes, located at the supports' axles (each on the ceramic or steel sides of the roller and the hinged supports), which are linked through a set of 6 flexible/stiff springs (one for each DOF) in order to impose the desired restrictions. In particular, stiff springs have been assigned to all DOFs except rotation about the y-axis (for both supports) and vertical relative displacement (for the roller support only). Finally, the extra nodes are joined to sets of nodes which belong to the ceramic or steel walls by force-distributed elements. As boundary conditions, the displacement of the nodes of the top and bottom steel walls has been fully constrained. Such conditions are not realistic, but they have been assumed here to compare the results with previous analyses.

The effects of pressure, solid materials' own weight and thermal loads have been studied. Only hydrostatic pressure has been preliminarily considered, due to the lack of a detailed assessment of the pressure drop along the whole PbLi loops. Nevertheless, it is possible to estimate it with a certain degree of confidence. A major contribution is produced in the inlet and outlet manifolds. By addressing this characteristic problem of DCLL designs, Rhodes *et al* [23] proposed a correlation of the 3D MHD pressure drop in non-conducting ducts featuring a sudden expansion in an inertial-electromagnetic regime. The current Ha ($1.3 \cdot 10^4$), Re ($1.7 \cdot 10^5$) and N ($\sim 10^3$) are out of the ranges studied in that work ($1000 \leqslant Ha \leqslant 6570$, $1918.44 \leqslant N \leqslant 863\,298$ and $50 \leqslant Re \leqslant 2500$). Applying this correlation to the front channels of the present problem, a pressure drop in the inlet manifold -that should be similar to the outlet one- of 0.43 bar is obtained. Chen *et al* [24] calculated the 3D MHD pressure drop in a reduced-scale DCLL module with electrically insulated walls, using conditions (Ha, Re) more similar to the current ones, although with a higher expansion ratio ($\sim$6 vs 4.45). They determined a pressure drop of 1.23 and 1.16 bar in the inlet and outlet manifolds, respectively. Therefore, from these references, it is reasonable to assume a pressure drop of $\sim$2 bar in the whole segment. Apart, assuming fully-developed flow in the poloidal channels,

the pressure gradient with ZrO_2 walls would be of the order of 10^2 Pa m^{-1}, which would involve an almost insignificant contribution to the total segment pressure drop. Regarding the ex-vessel loop, a rough estimation of major and minor losses gives a value of 2 bar. Summing up the different contributions, a total value of 4 bar is obtained. The maximum value of the hydrostatic pressure is ∼13 bar. In consequence, despite the significance of the hydrodynamic pressure (including MHD), studying the effect of the hydrostatic pressure is relevant to evaluate the feasibility of keeping the mechanical integrity of the ceramic box.

In the evolution of the design towards the trade-off between the neutronic and mechanical objectives, different cases have been evaluated, whose characteristics and results are described in the following subsections.

4.1. Case 1: initial sizing of the ceramic box

The initial sizing of the walls, gap and PbLi channels (v1.0) has set the external ceramic walls thickness in 25 mm and the gap thickness in 10 mm. SiC has been used as material for the neutron transport analysis. Pure compositions have been used in every analysis reported in this work. However, after the first neutron transport analysis with SiC, ZrO_2 has been the reference material for the mechanical analysis, in both this and the rest of cases, due to its superior strength. The temperature-independent mechanical properties of EUROFER and ZrO_2 (density, Young's modulus and Poisson's ratio) have been respectively taken from [25] and [26]. The values of σ_0, V_0 and m have been taken from [27]. Two loading cases have been studied: (1) increase of temperature from T_{room} to $T_{\text{operation}}$; and (2) combination of internal PbLi pressure and own weight.

The mechanical integrity analysis has shown a very good response of the isostatic supporting system to thermal loads, with peak stresses as low as a few MPa (figure 9). It has also demonstrated an adequate performance under PbLi hydrostatic pressure (up to ∼13 bar) and own weight (figure 10). It must be noted that a probability of failure lower than 10^{-6} is considered as evaluation criterion. Just a few elements localized at the intersection of the toroidal stiffening wall and the lateral walls -near the 90° turn after the inlet- are close to such limit (figure 11). This is a critical position because the exerted pressure is among the highest and the distance between the toroidal wall and the front and bottom walls is long. In fact, the deformation of the lateral walls along the toroidal axis is maximum in this area.

Conversely, the thickness of the double wall has led to a TBR of 1.02, far from the target of 1.15. However, the requirements concerning shielding functions (displacements per atom, fluence and nuclear heating in the TF coils winding pack and the vacuum vessel) [28] have been fulfilled.

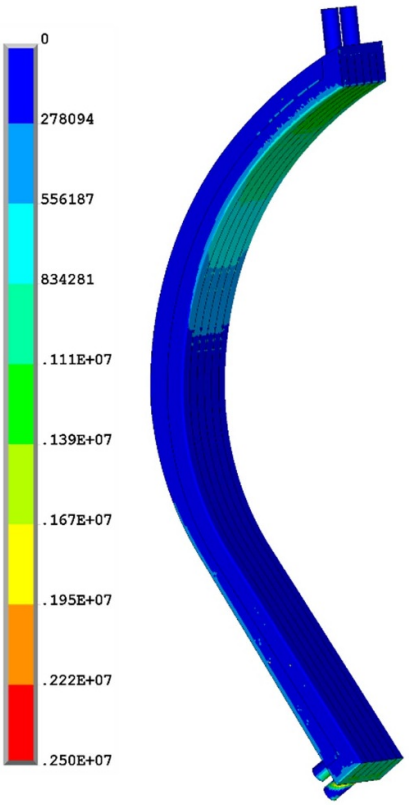

Figure 9. Equivalent stress (Pa) in the ceramic box due to thermal loads. Case 1.

4.2. Case 2: reduced wall and gap thickness

In order to improve tritium generation, the ceramic walls, gap and PbLi channels have been re-sized (v2.0). The external wall thickness has been reduced from 25 to 12.5 mm, the gap has been reduced from 10 to 5 mm, and the radial size of the PbLi front channels has been enlarged between 3 and 12%, depending on the kind of segment and the poloidal position.

As shown in figure 12, the re-sizing has resulted in a severe decrease in reliability when the ceramic box is loaded with PbLi hydrostatic pressure and its own weight. 3.38% of the FE model elements have a probability of failure higher than 10^{-6}. A mixture of cases 1 and 2 -case 2 b- (v1.0 model with v2.0 thickness) has been also analyzed to evaluate the respective contribution of the wall thickness and the PbLi channels size. The results show that the first is by far the most important factor to globally increment the probability of failure.

Regarding the neutronic assessments, the obtained TBR (1.144) is close to the target. The neutron transport analysis has been repeated, successively replacing SiC by $MgAl_2O_4$, SiO_2 and ZrO_2 (table 2). In the case of ZrO_2, the TBR increased to 1.17, a value with enough margin over the objective. With respect to the shielding responses, the three compositions fulfill the requirements, avoiding the TF coils quench. Only spinel overreaches the limit of nuclear heating in the TF coil, although a slight improvement in the shielding performance could be enough to meet the requirements.

4.3. Case 3: the chance of the gap gas

The gas that fills the gap offers a way to help the ceramic box withstanding the PbLi hydrostatic pressure without an undesirable increase of the wall thickness. This gas is meant to flow

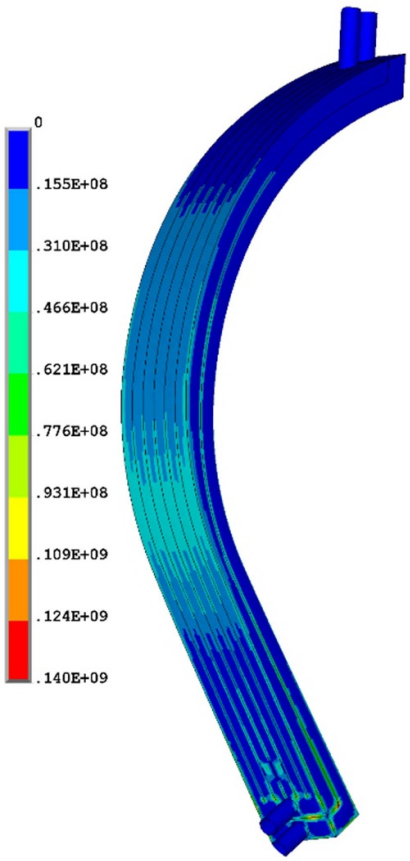

Figure 10. Equivalent stress (Pa) in the ceramic box due to PbLi hydrostatic pressure and own weight. Case 1.

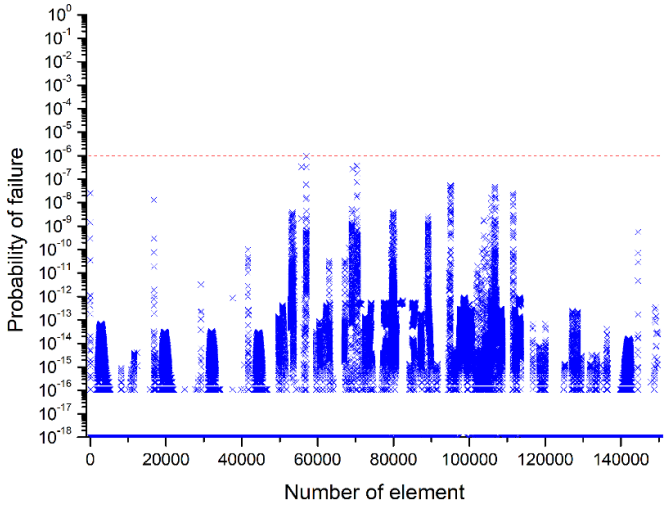

Figure 11. Probability of failure of each ceramic element of the FE model. Case 1.

at low or moderate velocity in order to drag gaseous activation products and help to smooth hot spots. In comparison with high-pressure gases, a low-pressure gas has lower density and hence, lower heat removal capacity, but it produces lower pressure drop and allows reducing the peak pressures generated on the ceramic surface in case of an accidental break of one of the FW He cooling channels [1]. With the aim of selecting

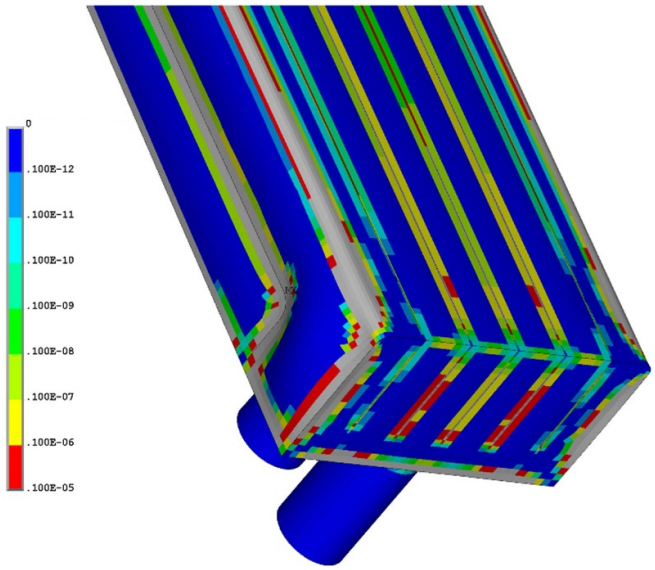

Figure 12. Probability of failure in the bottom region. Case 2.

Table 2. TBR results with different compositions. Case 2.

	TBR
SiC	1.144
$MgAl_2O_4$	1.14
SiO_2	1.15
ZrO_2	1.17

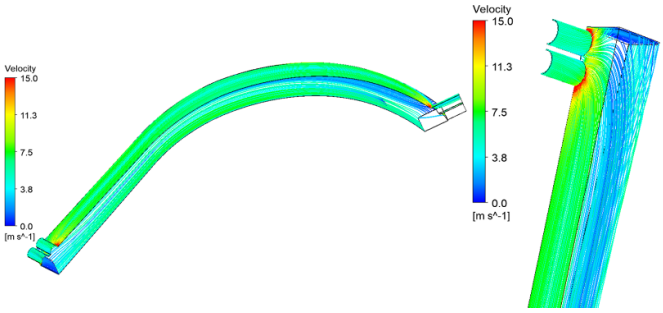

Figure 13. Velocity streamlines in the gap (He, 5 mm gap thickness, 5 m s^{-1} inlet velocity, p = 3 bar and isothermal case).

the operational conditions of this gas, a set of CFD simulations have been carried out in ANSYS FLUENT to evaluate the pressure drop and pumping power necessary in the OBC segment (figure 13). Different gases (He, N_2 and Ar), pressures (1 and 3 bar), inlet velocities (0.05, 1 and 10 m s^{-1}) and gap thicknesses (5 and 10 mm) have been assessed. The effect of temperature (isothermal and non-isothermal cases) has been also studied.

It has been found that the pressure losses and the pumping power are relatively low. In the worst case, the pumping power required for one segment is less than 4.5 kW, which can be supplied by a conventional blower. He, whose density and viscosity are the lowest, experiments the lowest pressure drops. Additionally, considering a non-uniform temperature

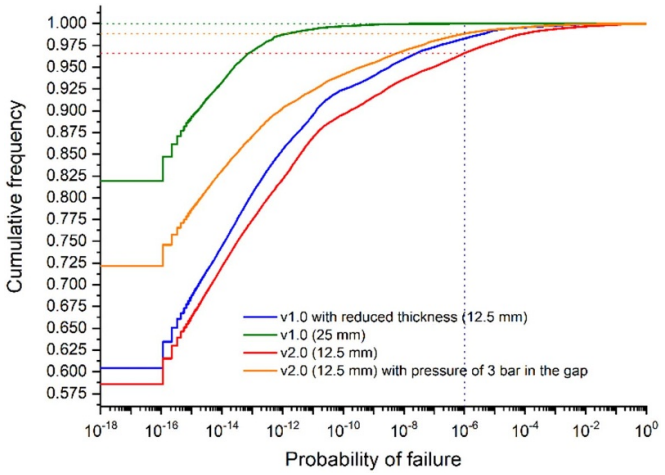

Figure 14. Cumulative frequency of elemental probability of failure in cases 1, 2, 2b and 3.

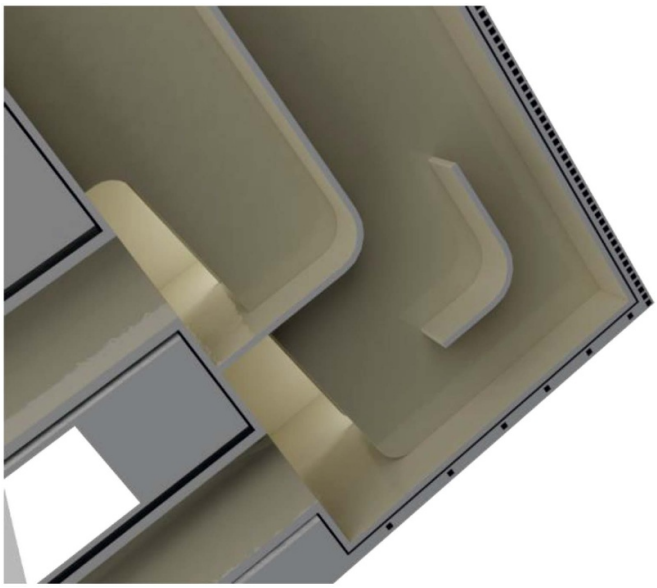

Figure 15. Detail of the auxiliary toroidal stiffening wall. Radial-poloidal section view.

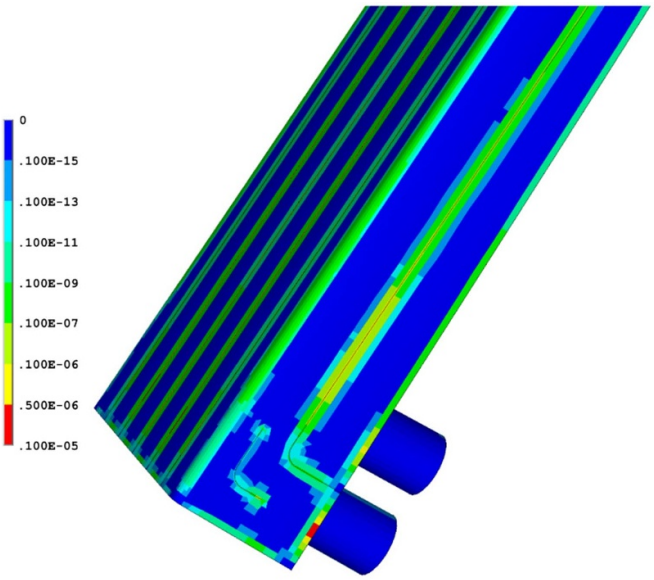

Figure 16. Probability of failure in the bottom region. Case 4.

involves an increase in pressure drop of ∼70%. Finally, the cooling ability of the gases at these conditions is not significant. Approximately 4 kW are extracted by He when an inlet velocity of 1 m s^{-1} is considered (around 40 kW with an inlet velocity of 10 m s^{-1}). These results indicate the possibility to moderately increase the gas pressure, so that it can oppose the PbLi hydrostatic pressure.

As can be perceived in figure 14 (orange vs. red curve), the effect of the gas pressure on the reliability of the ceramic box is not trivial, although insufficient for the tested level. Furthermore, such pressure level could be hardly raised, since it would mean increasing the load on the internal surface of a EUROFER FW without a stiffening grid.

4.4. Case 4: auxiliary toroidal stiffening wall

The last case of this series has consisted in increasing the lateral and back walls thickness from 12.5 to 22 mm, as well as increasing the front wall thickness from 12.5 to 14 mm. In addition, a new toroidal wall (12.5 mm thickness) has been included to strengthen the wide span at the 90° turn in the bottom region (figure 15). Such wall is not expected to have a significant impact on the PbLi flow, although it must be checked. This way, it is possible to stiff the largest unsupported areas without interposing thick walls which penalize the TBR. The positive mechanical effects are revealed in figure 16. Excepting one specific point, a probability of failure $<10^{-6}$ has been obtained in the whole number of elements. It must be emphasized that this analysis does not include the hydrodynamic pressure, although the overall result is still acceptable if an extra pressure of 4 bar is considered. In such case, only 0.8% of the total number of elements have a probability of failure $>10^{-6}$, which can be mitigated by minor measures.

From the neutronics point of view, this design provides a TBR of 1.154 (with ZrO_2), which fulfills the requirement. As can be appreciated in figure 17, when comparing the tritium generation gradient at the position of the auxiliary toroidal wall and other surrounding positions, this wall has a minor influence on the displacement of the local generation profile. The shielding requirements are fulfilled as well.

4.5. Reflectors and shielding materials to enhance the TBR

It has been also studied how to enhance the TBR by interposing a functional reflecting/shielding material between the EUROFER back wall and the ceramic box [29]. Looking for a material with a low neutron absorption cross section or a high elastic scattering cross section, different options (e.g. TiH_2, ZrH_2, $YH_{1.6}$, C, WC, B_4C) have been evaluated. It has been found that a C-based reflector can directly enhance the TBR (+1.58%). Besides, metal hydrides, preferably ZrH_2 -that also has a positive direct contribution to the TBR-, are useful to

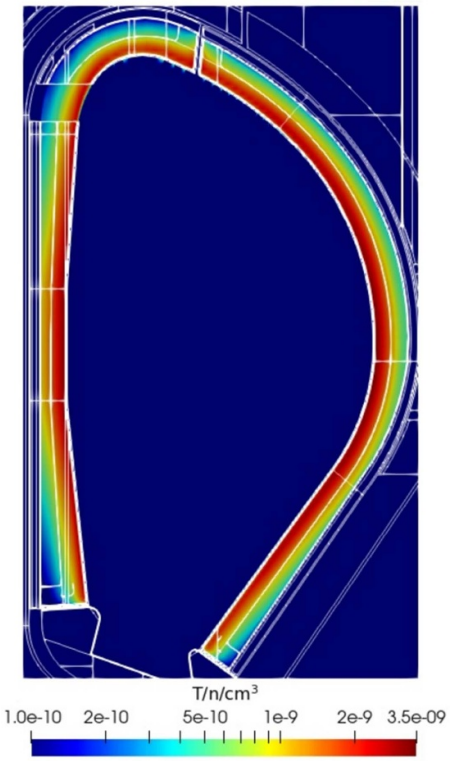

Figure 17. Tritium generation map for case 4. Radial-poloidal section view.

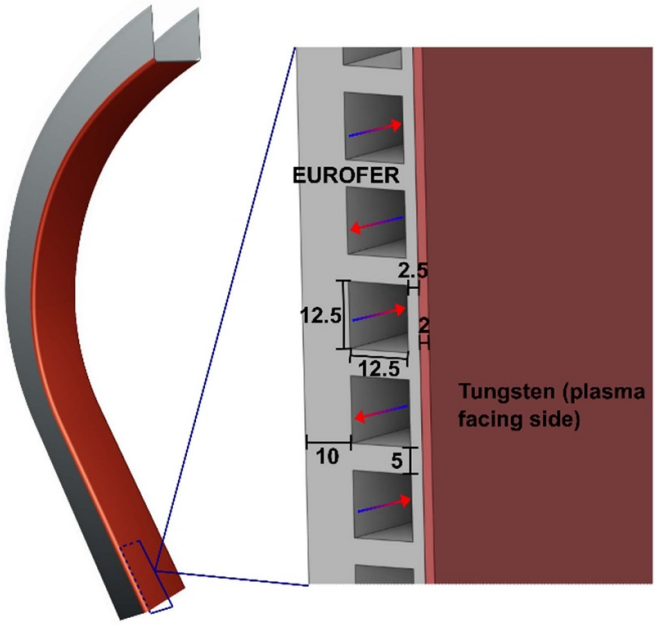

Figure 18. Detail of the FW cooling channels (poloidal-radial section view). The dimensions are indicated in mm. The blue-to-red arrows display the He flow direction.

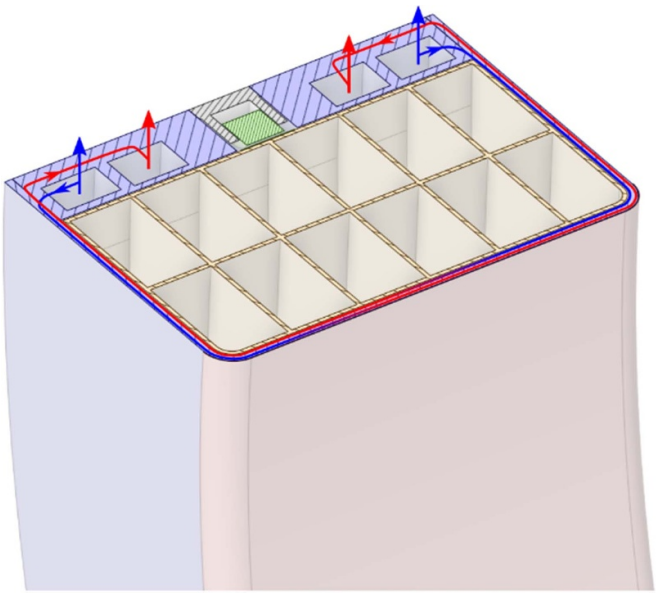

Figure 19. Scheme of manifolds (poloidal circulation) and U-shaped cooling channels (radial-toroidal-radial circulation) at the equatorial level. Two consecutive channels flowing in counterflow are represented.

reduce the shielding thickness in favor of the breeder one to increase the tritium production without modifying the ceramic box wall thickness.

5. Optimization of the FW cooling system

A substantial progress has been made in improving the thermal-hydraulic performance of the FW cooling system under steady state heat loads. The FW is cooled by a succession of square-section (12.5×12.5 mm^2) U-shaped channels in counterflow (figures 15 and 18) distributed along the poloidal direction by two long manifolds (figure 19). There is also a small number of channels in charge of cooling the top and bottom walls. Depending on the load specification, the steady state heat flux on the tungsten surface due to charged particles and radiation from the plasma can be very spatially-heterogeneous [30] (figure 20). The employ of a uniform mass flow rate adapted to the peak heat flux can lead to an oversizing of the cooling system that would decrease the thermodynamic cycle efficiency -helium extracts 1/3 of the total power deposited in the BB- and increase the coolant recompression power. For that reason, the TOMFLOW code has been developed and validated against 3D FE analysis [31]. It started from the basic strategy described in [1], based on the PLATOON code, and has incorporated additional phenomena. TOMFLOW allows a fast calculation of the minimum mass flow rate required in each channel to ensure that the EUROFER structure is kept at temperatures below 550 °C (figure 21). The results show a substantial gain in the global He outlet temperature (+18.5%) and a decrease in the total mass flow rate (−15.6%) in the OBC segment with respect to a uniform mass flow rate equal to the maximum demand.

However, that approach assumes that the channels are individually fed, with an ideal control of mass flow rate. The question is: if we consider the complete hydraulic networks, including the manifolds and channels, is it possible to modify the hydraulic resistance of each branch in a way that allows

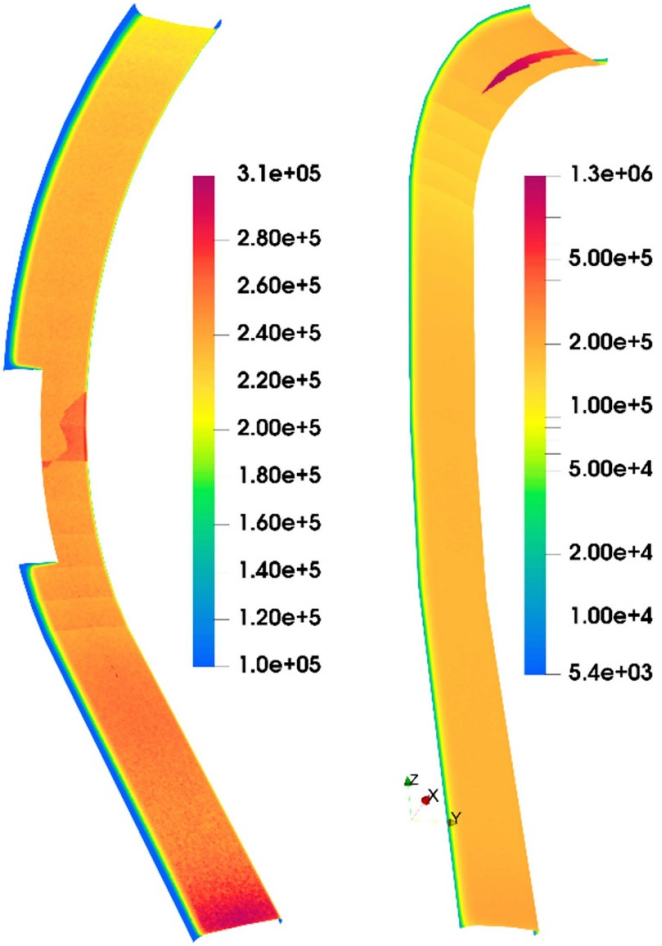

Figure 20. 3D steady-state heat flux map (W m^{-2}) on the surface of the OBC (left) and IB (right) FW at the end-of-flat equilibrium [30]. The OBC FW is partially covered by an equatorial limiter. To consider the most general case, it has been assumed here that the heat flux map in the limiter region would be symmetrical with respect the central radial-poloidal plane.

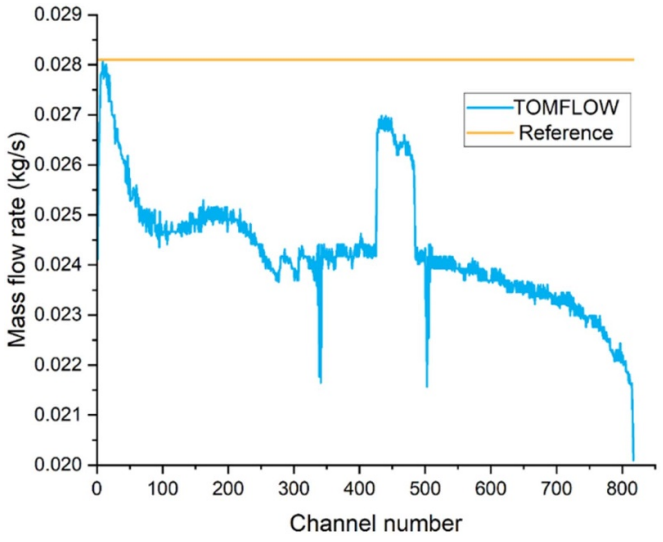

Figure 21. Minimum mass flow rate needed for each channel in the OBC segment.

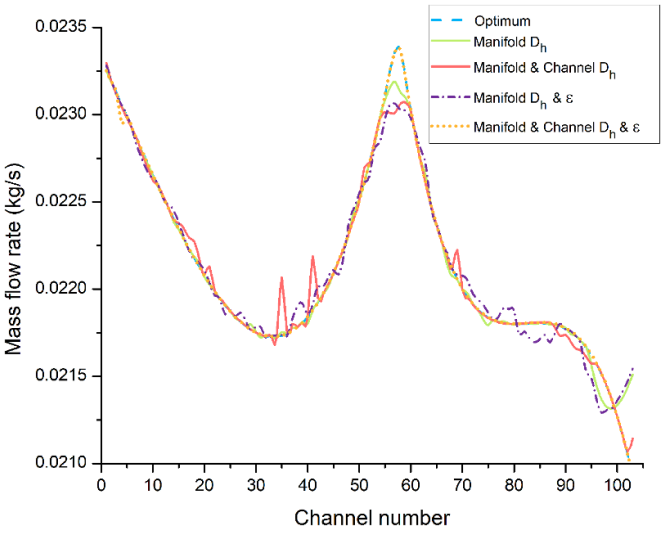

Figure 22. Comparison of the optimum mass flow rate (TOMFLOW) and the distribution obtained by GA in different cases.

reproducing the flow distribution obtained by TOMFLOW? In order to answer that question, an optimization based on Genetic Algorithms (GA) has been performed [32]. It is a computationally expensive procedure, so the optimization has been initially performed in a reduced model of 100 channels, in order to validate the methodology prior to implementing it in the whole geometry. In fact, the input has not been exactly the prediction obtained from TOMFLOW (figure 21), but a smooth curve adapted from it. As can be seen in figure 22, it has been possible to find several suitable configurations based on the combination of the variables that must be optimized. These include the dimensions of manifolds and channels and the surface roughness. The studied configurations approximate very well the flow distribution calculated by TOMFLOW. The best fit corresponds to the configuration with more variables.

Nevertheless, it is necessary to explore ways to enhance the computational efficiency and accelerate the convergence of the method. Future steps will involve the application of this methodology to the whole model, incorporating local minor losses and exploring solutions that allow a smoother variation of the hydraulic diameter along the manifolds length to improve the component manufacturability.

6. Modeling tritium transport

In section 2, it is affirmed that tritium permeation through the ceramic wall should be negligible because ceramic materials like SiC, ZrO_2 or Al_2O_3 generally have low permeability to H-isotopes. Nevertheless, this statement must be specified for different conditions and should be redefined to include the whole BB system. Using the simulation tool EcosimPro [33, 34], a system-level transient model of the blanket and the main ancillary systems that compose the PbLi loop has been created (figure 23). The model includes a blanket sector (1/16 of the tokamak) connected to two different loops: one for the IB

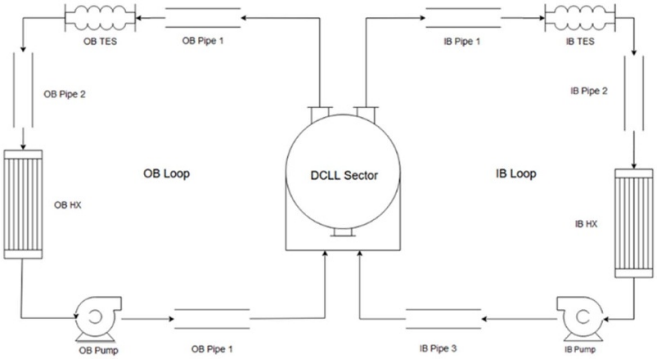

Figure 23. Process flow diagram of the BB tritium transport model.

segments and other for the OB segments. The segment submodel represents the PbLi channels, the ceramic walls and the gas that fills the gap with the EUROFER envelope (argon has been assumed here). The ancillary systems comprise a Permeator Against Vacuum (PAV) as tritium extraction system and a Steam Generator (SG). The different systems are connected by pipes.

The considered transport phenomena [33] are the following:

(a) PbLi flow: it represents the evolution of H-isotopes concentration. It includes advection terms, a source term and a permeation term.
(b) H-isotopes flux through materials: diffusion is governed by Fick's 1st law in function of the concentration gradient. It includes a trapping model.
(c) Interfaces between materials: application of the Sieverts' law at solid-solid and solid-liquid interfaces. In gas-solid interfaces there is a permeation flux determined by recombination and dissociation processes. This kind of boundary condition is also assigned to the external faces of the pipes, in order to consider permeation to the environment (room).

The materials considered in the model are PbLi, SiC (ceramic walls), EUROFER (pipes), AISI 316 (SG) and vanadium (PAV membranes). Their respective tritium transport properties have been taken from [35–42]. Tritium is generated with a rate of 320.26 g d^{-1} in pulses of 7200 s with a dwell time of 600 s [43]. Different cases have been analyzed:

6.1. Case 0: ideal extraction

It has been assumed an extraction efficiency of 80% in the PAV. Besides, the ceramic walls have been considered as non-damaged. The results show that the tritium inventory is mainly localized in the BB, although inventories in pipes and the SG are also important. Permeation losses occur principally in the SG (from PbLi to water). Permeation to the environment is also significant, but it is practically null inside the BB (from PbLi to Ar, figure 24), which absolutely agrees with the statement that opens this section.

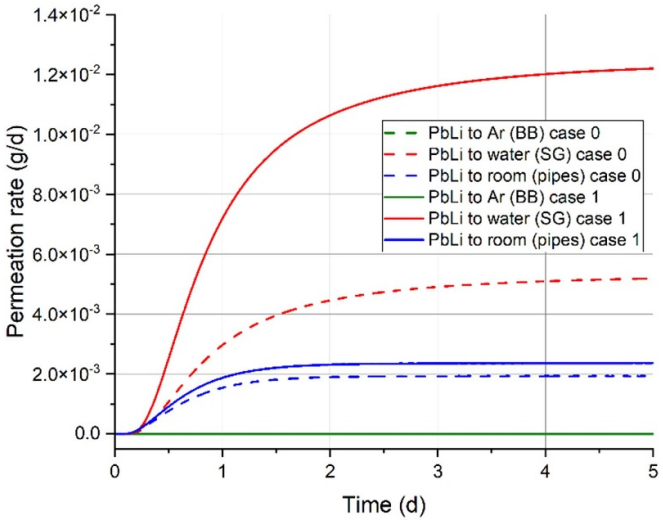

Figure 24. Evolution of permeation rates from the different subsystems. Cases 0 and 1.

6.2. Case 1: physical model of the PAV

The PAV submodel has been used instead of the ideal extraction efficiency. The calculated efficiency is different for each PbLi loop and, in any case, lower than the ideal one (approximately between 65 and 78%). Due to the high solubility of the PAV membranes, the PAV submodel retains the largest inventory in the system. As in case 0, the most important permeation losses occur in the SG (figure 24).

6.3. Case 2: damage factor

This case considers enhanced permeability in the ceramic material due to neutron damage. The effect of the damage factor (α) is distributed among diffusivity and solubility (factor $n \in [0, 1]$),

$$D_{\mathrm{dmg}} = \alpha^{n} D_0$$

$$Ks_{\mathrm{dmg}} = \alpha^{n-1} Ks_0$$

where D is the diffusivity and Ks is the Sieverts' constant.

It has been found that the neutron damage has to increase the mass transport properties of the ceramic seven orders of magnitude ($\alpha = 10^7$) to obtain a permeation rate of approximately 1 g d^{-1} in the BB (from PbLi to Ar).

6.4. Cases 3/1 and 3/2: H_2 in water or Ar

These cases are focused on assessing the effects of co-permeation and counter-permeation [44, 45]. The simulations start from the conditions of case 2 (damaged ceramic wall). The results of case 3/1 indicate that the tritium permeation rate in the SG depends on the H_2 concentration in water (figure 25). H_2 favors permeation by facilitating surface recombination. However, the increase of H_2 concentration in PbLi (permeated from water) enhances permeation to the environment but also

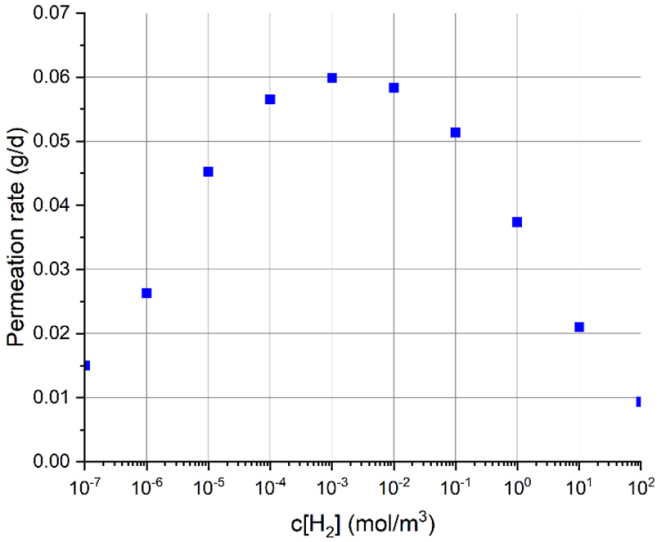

Figure 25. Tritium permeation rate in the SG (from PbLi to water). Case 3/1.

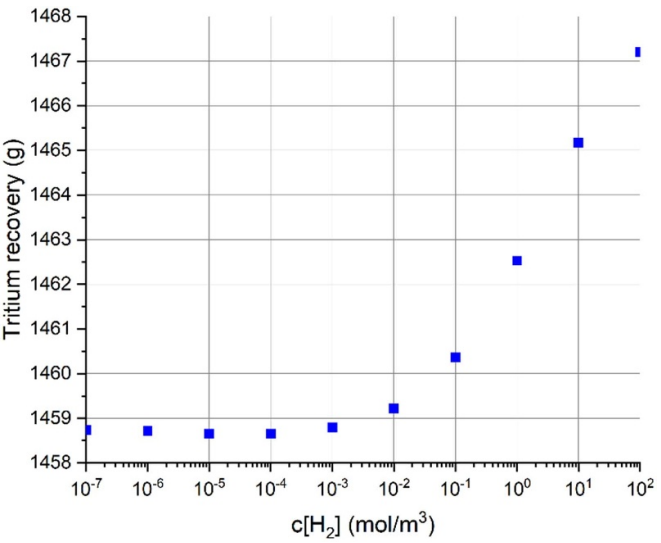

Figure 26. Tritium recovered in PAV after 5 d for a range of H_2 concentrations in water. Case 3/1.

facilitates tritium recovery in the PAV (figure 26). Indeed, for a sufficiently high concentration of H_2 in water, the tritium inventory in PbLi significantly decreases and counteracts the co-permeation effect in the SG. A similar extraction enhancement is observed when H_2 is added to Ar (case 3/2).

6.5. Case 4: trapping in the ceramic material

This case has been defined to assess the effect of considering trapping inside the SiC walls. According to [46–48], the thermal desorption spectrum of SiC is compatible with 2 or 3 high-temperature and high-density traps. They correspond to covalent bonds between tritium, carbon and silicon (C–Si–T, C–C–T and Si–C–T [49]).

For undamaged walls, the diffusion of tritium through the SiC bulk is so reduced that only a negligible amount of tritium is trapped. In case of heavily damaged walls ($\alpha = 10^7$), tritium can penetrate into the walls in significant quantities, where it is trapped in the high-temperature and high-density traps. In this extreme case, the trapped inventory after 20 d of operation would be more than 25% of the generated tritium. As expected, permeation rates in the pseudo-steady state are not affected by trapping phenomena.

In summary, the favorable situation under the reference conditions can get complicated by the presence of damage in the ceramic material (e.g. due to neutron irradiation), although the damage has to be severe to observe a significant tritium permeation from PbLi to the gap gas. Besides, the addition of H_2 to the SG water or the gas is revealed as an interesting resource to reduce tritium permeation rates from PbLi by improving tritium recovery.

7. MHD modeling activities

A 2D fully-developed flow code and a 1D fully-developed flow Q2D model have been created and extensively exploited to parametrically analyze heat transfer phenomena in buoyant liquid metal MHD flows. The models have reproduced in a simplified way one of the PbLi poloidal front channels of the OBC segment, assuming perfectly insulated walls.

The resolution of a high number of cases in HPC Marconi has allowed obtaining different correlations of the Nusselt number: with channel aspect ratio, wall conductance, Grashof (Gr), Hartmann (Ha), Reynolds (Re) and the exponent of the heat generation profile. The details are described in [50].

Apart, taking advantage of the PbLi-compatibility experiments with Al_2O_3 samples carried out in a forced circulation loop, which are cited in section 3, it has been proposed to numerically investigate the wall shear stress ($\tau = \mu \cdot \partial u/\partial z$, where μ is the PbLi dynamic viscosity and $\partial u/\partial z$ is the velocity gradient normal to the wall) at different flow velocities (1–41 cm s^{-1}) with and without an applied magnetic field (0–5 T). The objective has been to relate it back to the corrosion level of the retrieved samples, since previous works have correlated this magnitude with the thinning rate in water pipes [51]. ANSYS FLUENT has been used to model these experiments, employing the magnetic induction method and the SST k-ω as turbulence model.

As schematically represented in figure 27, two rows of samples are installed along the PbLi flow direction inside an electrically conducting duct. The magnetic field is perpendicular to the flow direction. Figure 27 also depicts a section of the mesh (~2 M of hexahedral cells). The steel walls are represented by a thin-wall boundary condition.

A relatively wide range of Re (up to ~32 000) and Ha (up to ~1600) have been simulated to investigate the impact of the flow regime on the wall shear stress. Figures 28 and 29 show the different velocity distribution obtained in the middle ZX plane for the cases with $B = 0$ and $B = 5$ T, respectively.

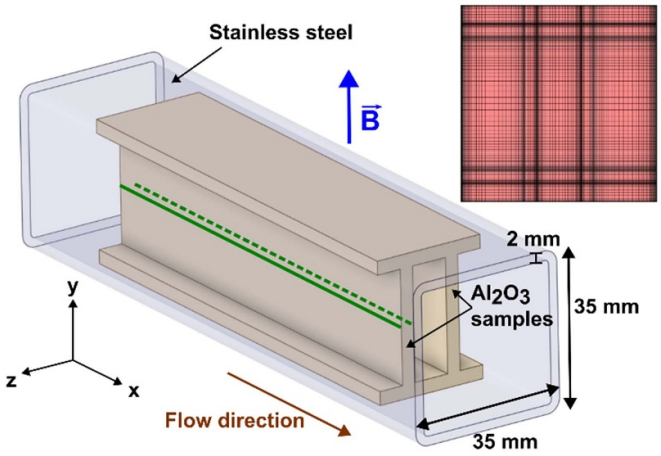

Figure 27. Geometry of the model. The mesh is shown on the right side. The lines along which the wall shear stress is evaluated are displayed in green (solid: outer side; dotted: inner side).

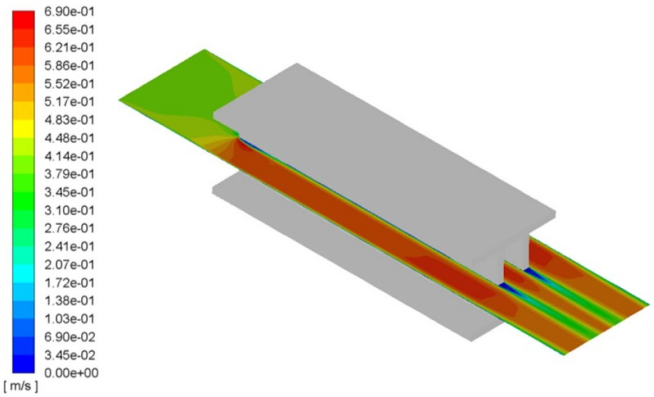

Figure 28. Velocity map in the middle plane at B = 0 and an average velocity of 41 cm s^{-1}.

Figure 30 exposes the average wall shear stress calculated in the outer side line of figure 27 as a function of Re and Ha. The graph clearly exhibits a greater dependence of this magnitude with Re than with Ha for the range of values explored. When both dimensionless numbers are combined into the Stuart number or interaction parameter ($N = Ha^2/Re$), the plot of the wall shear stress against this number (figure 31) shows a power law tendency. Translating the numerical findings into the corrosion level of the Al_2O_3 samples, the analysis of such samples should show 30%–58% higher erosion in the surfaces localized inside the 5 T magnetic field than the ones localized outside, depending on the sample side (inner or outer, respectively) in which the analysis is done. Nevertheless, the microstructure has remained practically unaltered, independently of the sample position with respect to the magnetic field. Therefore, this hypothesis could not be verified.

To conclude this section, it must be mentioned an ongoing activity that looks for studying the flow distribution among the parallel channels from the inlet pipes, which potentially can have a significant impact on the design (e.g. need of flow deflectors).

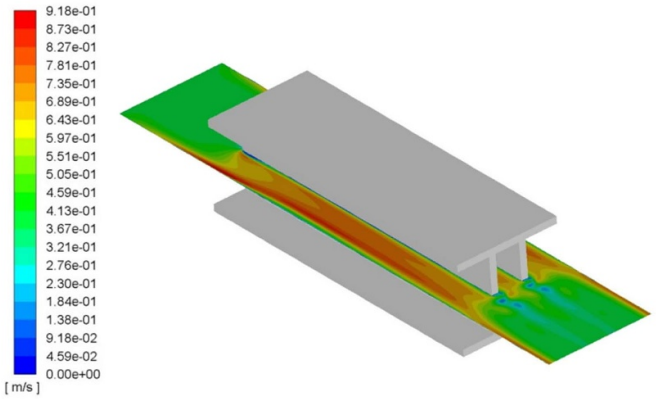

Figure 29. Velocity map in the middle plane at B = 5 T and an average velocity of 41 cm s^{-1}.

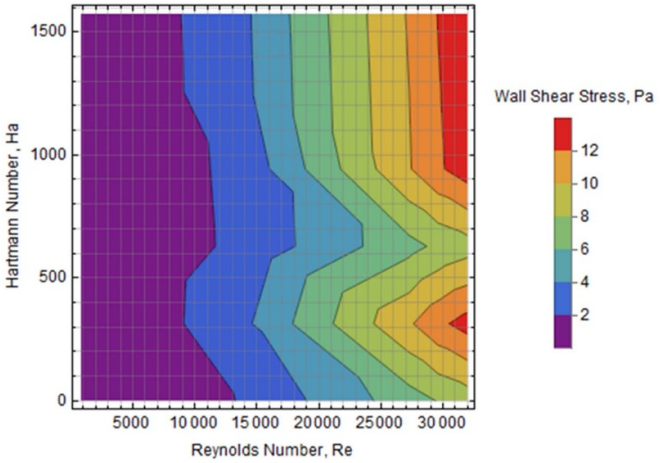

Figure 30. Wall shear stress as a function of Re and Ha in the outer wall line.

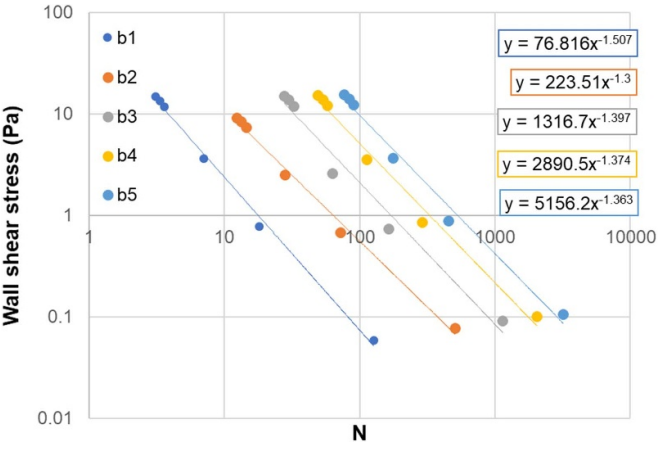

Figure 31. Wall shear stress obtained in the outer side of the samples wall in function of the Stuart number (N).

8. Conclusions

The proposed design of an advanced BB is based on an evolution of the DCLL concept. In a summary of the advantages

that have motivated its conception, it is worth noting the ones derived from the integration of a ceramic breeding zone and a protecting steel envelope that includes the FW. The electrically resistive and chemically compatible ceramic material allows minimizing the MHD pressure drop and corrosion-erosion rate, and means lower weight and lower steady state magnetic forces due to magnetization of the reduced activation ferromagnetic steel. Besides, it makes tritium permeation towards the exterior of the box almost negligible. Such integration of the ceramic box and the steel envelope allows a simultaneous operation with two thermal levels and minimizing the fraction of thermal power extracted by He, a compressible fluid with larger needs in recirculating power than the self-cooled breeder, PbLi. Precisely, the configuration of the PbLi channels minimizes the risk of reversed flows due to buoyancy forces and the problems linked to nucleation and growing of He bubbles. Furthermore, the broad temperature range selected for these circuits (300 °C–700 °C) is favorable to reduce the mass flow rate (better to minimize MHD and pumping power) and still permits achieving a significant value of Carnot's cycle efficiency. The high outlet temperature of PbLi is also beneficial to improve the recovery of tritium dissolved in the liquid metal.

Among the drawbacks, the double-wall thickness supposes a challenge for tritium self-sufficiency, although it has been demonstrated that is possible to find solutions that satisfy tritium production and shielding requirements and, at the same time, safeguard the blanket mechanical integrity. The need of developing ceramic-metallic connections for the interfaces between the blanket and the ex-vessel pipes, which is already an ongoing activity, is another difficulty. In general, manufacturing can be complex, because of the size of the ceramic box and the need of ensuring homogeneous properties in the whole volume. Like in the case of other BB concepts that propose analogous designs of the FW, this component faces critical obstacles in manufacturing (deposition of the W layer in a large curved area and assembly of the steel parts while keeping the specifications of the cooling channels).

The R&D activities have been focused on the characterization of candidates for the ceramic material. So far, no serious showstopper in terms of electrical conductivity and compatibility with PbLi (in as-received or irradiated/implanted conditions) of some commercial compositions has been found.

Acknowledgments

This work has been carried out within the framework of the EUROfusion Consortium, funded by the European Union via de Euratom Research and Training Programme (Grant Agreement No. 101052200—EUROfusion). Views and opinions expressed are however those of the author(s) only and do not necessarily reflect those of the European Union or the European Commission. Neither the European Union nor the European Commission can be held responsible for them.

This work has been partially supported by the computing facilities of Extremadura Research Centre for Advanced Technologies (CETA-CIEMAT), funded by the European Regional Development Fund (ERDF). CETA-CIEMAT belongs to CIEMAT and the Government of Spain.

This work has been also partially supported by Comunidad de Madrid under TECHNOFUSION(III)-CM, S2018/EMT-4437.

The authors would like to thank the FDS Team for providing SuperMC, a general, intelligent, accurate and precise simulation software system for design and safety evaluation of nuclear systems.

ORCID iDs

I. Palermo https://orcid.org/0000-0001-8725-8167
F.R. Urgorri https://orcid.org/0000-0002-3261-1135
D. Rapisarda https://orcid.org/0000-0003-0272-729X
J. Alguacil https://orcid.org/0000-0002-5663-215X
J.M. García https://orcid.org/0000-0002-0106-8694
M. Roldán https://orcid.org/0000-0003-1695-2199
A. Rueda https://orcid.org/0009-0005-9293-9617
D. Sosa https://orcid.org/0009-0000-5319-5575

References

[1] Fernández-Berceruelo I. *et al* 2021 *Fusion Eng. Des.* **167** 112380
[2] Rapisarda D., Fernández-Berceruelo I., García A., García J.M., Garcinuño B., González M., Moreno C., Palermo I., Urgorri F.R. and Ibarra A. 2021 *Nucl. Fusion* **61** 115001
[3] Zinkle S.J. and Ghoniem N.M. 2011 *J. Nucl. Mater.* **417** 2–8
[4] Smolentsev S., Morley N.B., Abdou M.A. and Malang S. 2015 *Fusion Eng. Des.* **100** 44–54
[5] Siriano S., Balcázar N., Tassone A., Rigola J. and Caruso G. 2022 *Fluids* **7** 152
[6] Smolentsev S., Rhodes T., Pulugundla G., Courtessole C., Abdou M., Malang S., Tillack M. and Kessel C. 2018 *Fusion Eng. Des.* **135** 314–23
[7] Fernández-Berceruelo I. and Rapisarda D., 2022 An approach for the pathway towards the development of high performance breeding blankets *8th IAEA DEMO Workshop*, (*Vienna (Austria), 30 August – 02 September 2022* (available at: https://conferences.iaea.org/event/298/)
[8] Kovari M. 2017 EUROfusion internal report EFDA_D_2NDSK, DEMO1 reference design—output from PROCESS
[9] Mergia K. and Boukos N. 2008 *J. Nucl. Mater.* **373** 1–8
[10] Shercliff J.A. 1953 *Math. Proc. Camb. Phil. Soc.* **49** 136–44
[11] Martelli D., Venturini A. and Utili M. 2019 *Fusion Eng. Des.* **138** 183–95
[12] Miyazaki K., Inoue S., Yamaoka N., Horiba T. and Yokomizo K. 1986 *Fusion Technol.* **10** 830–6
[13] Palermo I., Mauricio Garcia J., González M., Malo M. and Rapisarda D. 2022 *Nucl. Mater. Energy* **30** 101136
[14] González M. *et al* 2020 *Fusion Eng. Des.* **159** 111761
[15] Petráš R. *et al*. 2021 Flexural strength of ceramic material in liquid Pb-16Li at elevated temperatures *ICFRM-21* (*Granada (Spain), 22–27 October 2023*) (available at: www.icfrm-21.com/)
[16] Petráš R., Kordač M., Chocholoušek M. and Vála L. 2023 *Fusion Eng. Des.* **189** 113474
[17] García J.M., González M. and Sánchez F. 2022 *Fusion Eng. Des.* **184** 113309
[18] Patiño J. *et al* 2023 The chemical compatibility of oxide ceramic candidates in static PbLi for the advanced DCLL

ISFNT-15 (*Las Palmas de Gran Canaria (Spain)*, *10–15 September 2023*) (available at: https://isfnt2023.com/)
[19] González M. *et al* 2023 Towards the down-selection of ceramic materials for the European high temperature DCLL BB concept based on single module segments (SMS) *ISFNT-15* (*Las Palmas de Gran Canaria (Spain)*, *10–15 September 2023*) (available at: https://isfnt2023.com/)
[20] Fischer U., Boccaccini L.V., Cismondi F., Coleman M., Day C., Hörstensmeyer Y., Moro F. and Pereslavtsev P. 2020 *Fusion Eng. Des.* **155** 111553
[21] X-5 Monte Carlo Team MCNP–A general Monte Carlo n-particle transport code, version 5
[22] Bermejo R. and Danzer R. 2014 Mechanical characterization of ceramics: designing with brittle materials *Comprehensive Hard Materials* vol 2 (Elsevier) pp 285–98
[23] Rhodes T., Smolentsev S. and Abdou M. 2018 *Phys. Fluids* **30** 057101
[24] Chen L., Smolentsev S. and Ni M.-J. 2020 *Nucl. Fusion* **60** 076003
[25] Gillemot F. *et al* 2016 EUROfusion internal document EFDA_D_2MT9X8, DEMO Material Property Handbook: pilot Project on EUROFER97
[26] Kyocera Technical data for zirconia (available at: https://global.kyocera.com/prdct/fc/list/material/zirconia)
[27] Wirwicki M. 2018 *Two Parametric Analysis of the Weibull Strength of Advanced Ceramic Materials* (UTP University of Science and Technology)
[28] Fischer U., Bachmann C., Palermo I., Pereslavtsev P. and Villari R. 2015 *Fusion Eng. Des.* **98–99** 2134–7
[29] Palermo I., Rapisarda D. and Sosa D. 2022 Advanced shielding and reflector materials to enhance the HT DCLL BB for the EU-DEMO fusion reactor *14th ICRS* (*Seattle (USA)*, *25–29 September 2022*) (https://doi.org/10.13182/ICRSRPSD22-39097)
[30] Gerardin J. and Firdaouss M. 2018 Radiative and charged particles heat load on design 6, *EUROfusion internal document* EFDA_D_2NHLYG
[31] Noguerón J.A., Fernández-Berceruelo I. and Rapisarda D. 2022 A study of the optimal cooling of the first wall for the SMS DCLL breeding blanket *32nd SOFT* (*Dubrovnik (Croatia)*, *18–23 September 2022*) (available at: https://soft2022.eu/)
[32] Noguerón J.A., Fernández-Berceruelo I. and Rapisarda D. 2023 Adaptation of the first wall cooling circuits to achieve an efficient distribution of the coolant flow in the SMS DCLL breeding blanket (*ISFNT-15*) (*Las Palmas de Gran Canaria (Spain) 10–15 September 2023*) (available at: https://isfnt2023.com/)
[33] Urgorri F.R., Moreno C., Carella E., Rapisarda D., Fernández-Berceruelo I., Palermo I. and Ibarra A. 2017 *Nucl. Fusion* **57** 116045
[34] Gilardi T., Moreno C. and Grisolia C. 2021 *Fusion Eng. Des.* **166** 112278
[35] Chan Y.C. and Veleckis E. 1984 *J. Nucl. Mater.* **122–123** 935–40
[36] Verghese C.K., Zumwalt L.R., Feng C.P. and Elleman T.S. 1979 *J. Nucl. Mater.* **85–86** 1161–4
[37] Causey R.A., Wampler W.R., Retelle J.R. and Kaae J.L. 1993 *J. Nucl. Mater.* **203** 196–205
[38] Esteban G.A., Peña A., Urra I., Legarda F. and Riccardi B. 2007 *J. Nucl. Mater.* **367–370** 473–7
[39] Esteban G.A., Perujo A., Sedano L.A. and Mancinelli B. 2000 *J. Nucl. Mater.* **282** 89–96
[40] Forcey K.S. 1998 *J. Nucl. Mater.* **160** 117–24
[41] Malo M., Peñalva I., Azkurreta J., Garcinuño B., Liu H.-D., Rapisarda D., Zhou H.-S. and Luo G.-N. 2022 *Membranes* **12** 579
[42] Steward S.A. 1983 Review of hydrogen isotope permeability through materials *Technical Report for LLNL,* UCRL-53441*, ON:*DE84007362
[43] Spagnuolo G.A. *et al* 2021 *Fusion Eng. Des.* **173** 112933
[44] Kizu K. and Tanabe T. 1998 *J. Nucl. Mater.* **258** 1133–7
[45] Kizu K., Pisarev A. and Tanabe T. 2001 *J. Nucl. Mater.* **289** 291–302
[46] Oya Y., Onishi Y., Okuno K. and Tanaka S. 2005 *Mater. Trans.* **46** 552–6
[47] Oya Y. *et al* 2002 *Phys. Scr.* **103** 81–84
[48] Oya Y., Onishi Y., Kodama H., Okuno K. and Tanaka S. 2002 *J. Nucl. Mater.* **337–339** 595–59
[49] Sugiyama T., Morimoto Y., Iguchi K., Okuno K., Miyamoto M., Iwakiri H. and Yoshida N. 2002 *J. Nucl. Mater.* **307–311** 1080–3
[50] Suàrez D. *et al* 2023 arXiv:2303.11478
[51] Utanohara Y., Nagaya Y., Nakamura A., Murase M. and Kamahori K. 2013 *J. Power Energy Syst.* **7** 138–47